lubricants

MDPI

Article

Study on Leakage Performance and Rotordynamic Characteristics of a Novel Semi-Y Type Labyrinth Seal

Huihao Su [1], Junlin Shi [2] and Wenjie Zhou [1,*]

[1] School of Energy and Power Engineering, Jiangsu University, Zhenjiang 212013, China
[2] School of Mechanical Engineering, Sichuan University of Science & Engineering, Zigong 643000, China
* Correspondence: zhouwenjiezwj@ujs.edu.cn

Abstract: A new type of labyrinth seal with semi-Y of rotor teeth (SYLS) is proposed in this paper. The rationality and accuracy of the numerical model are validated by the experimental results, and the static characteristics are investigated. Furthermore, the effects of pressure drop, rotation speed, tilt angle, and tip clearance on the dynamic coefficients and stability are also studied in detail. The results imply that the novel SYLS structure generally has better leakage and stability performance compared with the traditional labyrinth seal. The maximum error applied in the numerical simulation is only 2.81%, and the worst leakage occurs when the tilt angle is 70° for the SYLS structure due to the smaller vortex dissipation. Moreover, the novel SYLS structure shows the best stability when the tilt angle is 45°. The novel SYLS structure and corresponding results can provide a reference for the research and design for labyrinth seal and the application of centrifugal pump.

Keywords: semi-Y labyrinth seal; leakage performance; whirl frequency ratio; dynamic coefficients

check for updates

Citation: Su, H.; Shi, J.; Zhou, W. Study on Leakage Performance and Rotordynamic Characteristics of a Novel Semi-Y Type Labyrinth Seal. *Lubricants* **2022**, *10*, 234. https://doi.org/10.3390/lubricants10100234

Received: 14 August 2022
Accepted: 22 September 2022
Published: 24 September 2022

Publisher's Note: MDPI stays neutral with regard to jurisdictional claims in published maps and institutional affiliations.

1. Introduction

The inner flow, including gap flow, plays an important role in the efficiency and operational security of the pump system [1–4]. The annular seals are generally used to resist leakage and are mainly classified as smooth seals, annular grooved seals, labyrinth seals, brush seals, floating seals, etc. The labyrinth seal, the most common type of annular seal, has the advantage of non-contacting, low friction, simple structure, and high reliability compared with other annular seals.

The leakage performance is a major characteristic of annular seals and depends on seal geometry and operating conditions. For seal geometry, most studies [5–7] indicated that a smaller clearance means a lower leakage. However, Hur et al. [8] presented that the variation of leakage was not monotonous with the increase in clearance size in the stepped labyrinth seal. In other words, there was an optimum clearance to minimize the leakage of the stepped labyrinth seal. There are three common structures in labyrinth seals, the teeth on the rotor seal (TOR), the teeth on the stator seal (TOS), and the interlocking seal (ILS), with the ILS structure having the lowest leakage [9]. Based on this structure, Zhang et al. [10] presented a mixed labyrinth seal with lateral teeth, which reduced the leakage by about 30% compared with the ordinary ILS. Woo et al. [11] investigated the leakage performance of the helical grooved pump seal. The results showed that the helical groove on both the stator and the rotor has better leakage performance than on the stator or the rotor. Wróblewski et al. [12,13] presented the optimization of straight-through labyrinth seals with different land structures and performed the experimental validation. The reduction in leakage of optimal structure reached 18% in comparison to the reference configuration. In addition, many studies [14–17] found that the pressure drop is a key parameter for leakage performance, and the higher the pressure drop, the more leakage will result. Nagai et al. [18] studied the influence of rotation on leakage in the partially helically grooved seal and pointed out that the leakage flow reduced as rotation speed increased.

The dynamic characteristic and stability of the annular seal are the other factors that have been investigated extensively in previous studies, except for leakage performance. When the labyrinth seal works under error conditions, the reaction force of the labyrinth seal may induce fluid excitation and intensify rotor vibration, which could threaten the safety of the equipment. Li et al. [19] performed a comparison of rotordynamic performance for three types, TOS, TOR, and ILS, of labyrinth seals, and the TOS labyrinth seal revealed the best stability among the three seals. Zhang et al. [20] investigated the rotordynamic performance of a novel anti-stagnation labyrinth seal. The results showed that the stability of anti-stagnation had a positive tendency as the rotation speed and inlet pressure increased. Alex Morelandet et al. [21] measured the static and rotordynamic characteristics of a smooth-stator/grooved-rotor annular seal. The results showed that the whirl frequency ratio of smooth-stator/grooved-rotor seal is generally high, which means poorer stability characteristics. Zhang et al. [22] measured the influence of clearance on the rotor performance of a labyrinth seal in wet-gas conditions. They discovered that small clearance obtained high critical speed for inlet liquid volume fraction from 12% to 15%. Li et al. [23] compared the numerical results of rotordynamic characteristics for a pocket damper seal and a labyrinth seal with different inlet pre-swirls. They presented that the negative pre-swirl was a stabilizing factor that had a great development of effective damping and the positive pre-swirl generated the opposite function. However, the results of Zhang et al. [24] showed that a positive pre-swirl could enhance the stability of the labyrinth seal with few blades. Furthermore, Untaroiu et al. [25] proposed a novel labyrinth seal with swirl brakes designed to increase system stability. Their studies indicated that the swirl breaks effectively reduced circumferential velocity, which was related to destabilizing the cross-coupled stiffness coefficients. Wu et al. [26] presented the updated bulk-flow model from CFD (Computational Fluid Dynamics) steady flow results. The updated bulk-flow model delivered predictions with an accuracy comparable to the CFD results and lower time-consuming. In addition, some new types of seal, such as herringbone-grooved seal [27–29], T-type labyrinth seal [30], and staggered helical labyrinth seal [31], were applied for better rotordynamic performance.

In this work, a new type of structure is presented to minimize leakage based on ILS. The new type of seal with semi-Y of rotor teeth is called a semi-Y labyrinth seal (SYLS). Firstly, the numerical calculation model for the labyrinth seal is validated by the experimental results. Furthermore, the static characteristic of SYLS with various tilt angles of rotor teeth are investigated to evaluate the leakage performance. In addition, the research about rotordynamic performance, including the dynamic coefficients and whirl frequency ratio of SYLS, are calculated. The novel SYLS structure and corresponding results can provide a reference for the design of labyrinth seal and the application of centrifugal pump.

2. The Model of SYLS Structure

The present studies show a strong correlation between the tip clearance size and leakage because the size of the clearance determines the strength of the throttling effect. It is supposed that the boosted throttling and turbulence in the seal chamber are important to controlling leakage in this study. In contrast to traditional ILS, the novel SYLS structure changes the structure of the rotor tooth to create an inner clearance. Figure 1 presents the 3D model of the ILS structure and SYLS structure. The distinct difference between ILS and SYLS is that the rotor tooth of the former is vertical, while the rotor tooth of the latter is only partially vertical, and the rest is inclined towards the stator tooth.

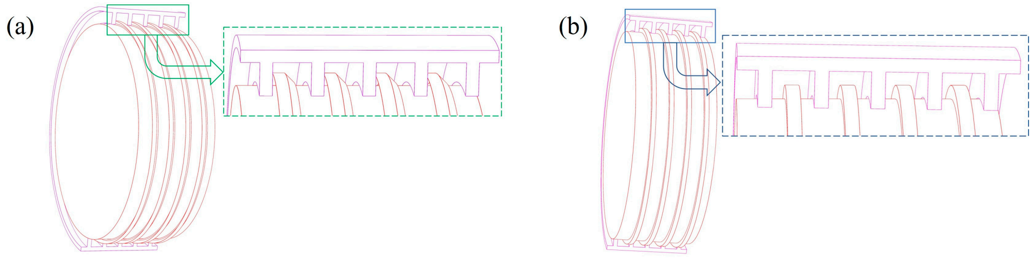

Figure 1. Three-dimensional model of labyrinth seal: (**a**) SYLS structure and (**b**) ILS structure.

3. Computational Method

3.1. Structural Dimension

Figure 2 shows the structural parameters of SYLS structure with a helical tooth, including tooth number Z, seal radial clearance C_r, seal length L, the distance between rotor teeth and static teeth L_p, rotor diameter D, rotor tooth height H_r, stator tooth height H_s, stator tooth height H_v, rotor tooth width B_r, stator tooth width B_s, and cavity width B_c. The corresponding values of structural parameters are listed in Table 1.

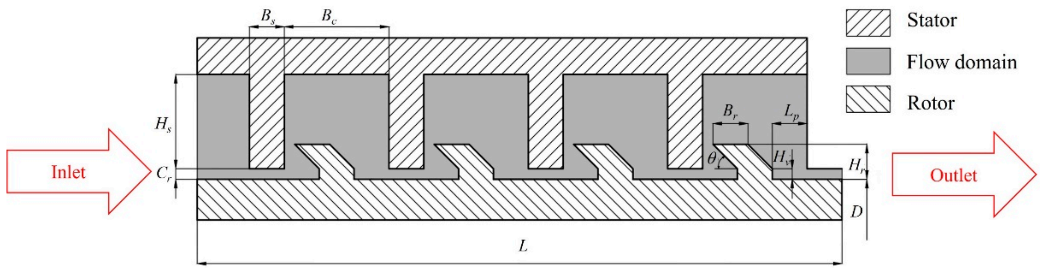

Figure 2. The structural parameters of SYLS structure.

Table 1. The values of SYLS structure with the helical tooth.

Seal Parameters	Z	C_r (mm)	H_s (mm)	H_r (mm)	H_v (mm)	B_s (mm)	B_c (mm)	B_r (mm)	L_p (mm)	L (mm)	D (mm)	θ (°)
Value	4	0.3	2.7	1	0.3	1	3	1	1	18.5	50	45

3.2. Solution Settings

The working medium is clear water. The two-equation turbulence model is commonly used to solve turbulent flow in labyrinth seals. The standard k-ε turbulence model of the two-equation turbulence model was usually selected to solve the performance calculation of the labyrinth seal since it has the advantage of great reliability and precision [31]. A scalable wall function is adopted in this study. The calculated Y+ value for all walls ranges from 0 to 50, well within the allowed range of a scalable wall function requirement. Moreover, the second-order upwind for turbulent kinetic energy and dissipation rate are chosen in this study for more precise results. The pressure drop Δp and rotation speed for boundary conditions are 0.2 MPa and 1450 rpm, respectively. In addition, the calculation results are assumed to converge when the residuals of all variables, especially the turbulent kinetic energy and dissipation rate, are approached 10^{-5}. The numerical parameters and the boundary conditions, which are imposed for the present investigation, are furnished in Table 2.

Table 2. Numerical details for the CFD analyses.

Numerical Parameters/Details	Specification
Rotation speed	1450 rpm
Inlet pressure	0.2 MPa
Outlet pressure	0 MPa
Wall properties	Smooth, adiabatic, no-slip
Turbulence model	Standard k-ε
Wall function	Scalable
Discretization	2nd order upwind scheme
Working medium	Clear water

3.3. Validation of the Computational Model

In order to verify the computational accuracy and reliability of the selected numerical method, the experimental results presented by Zhai et al. [27] are compared with the numerical simulation results. The herringbone-grooved seals consist of two groups of spiral grooves and a storage area. The two groups are in reverse direction, the upstream spiral part is situated on the high-pressure side, and the other downstream spiral part is located on the low-pressure side. The storage area is a narrow band to restrain the flow from upstream to downstream. The pressure difference is 0.142 MPa, and the rotation speed ranges from 360 rpm to 2400 rpm. The comparison results of the spiral labyrinth seal are shown in Figure 3. Obviously, the numerical simulation results calculated by standard k-ε turbulent model are in good agreement with experimental results. The maximum and minimum errors are 1.87% and 2.81%, respectively. Moreover, the leakage is steady with the increase in rotation speed. These results indicate that the standard k-ε turbulence model can be applied to capture the performance of labyrinth teeth structures.

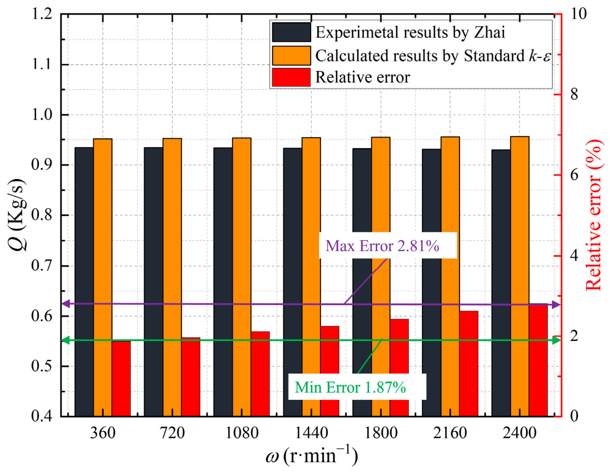

Figure 3. Leakage comparisons between experimental results and numerical results [27].

3.4. Mesh Independence Verification

The calculation precision and accuracy are mainly related to two aspects: the quality and quantity of mesh. On one hand, the particular location near the wall and small boundary were refined during the meshing process for acquiring high-quality meshes. Figures 4 and 5 show the refined computational meshes. The related structural parameters of ILS and SYLS refer to in Table 1. On the other hand, the computational results were independent of mesh when the density of mesh approaches a sufficiently large value. Therefore, the study on the variation of leakage and axial velocity with the increase in mesh number is proposed. The detailed results are displayed in Figure 6. As shown in Figure 6a, it can be seen that a smaller amount of mesh cannot accurately show the characteristics of clearance flow. The effect of the number of meshes on axial velocity near rotor surface between rotor teeth is shown in Figure 6b. As the number of mesh increases, the axial velocity distribution becomes more similar for the same structure. When considering the calculation's accuracy and time consumption, this paper takes a cell with 1,465,590 elements as the final computational mesh for ILS and a cell with 1,953,504 elements for SYLS, respectively.

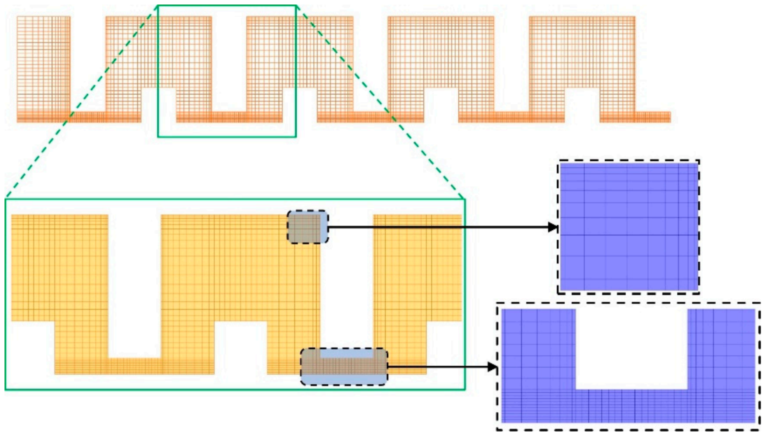

Figure 4. Mesh structure of ILS.

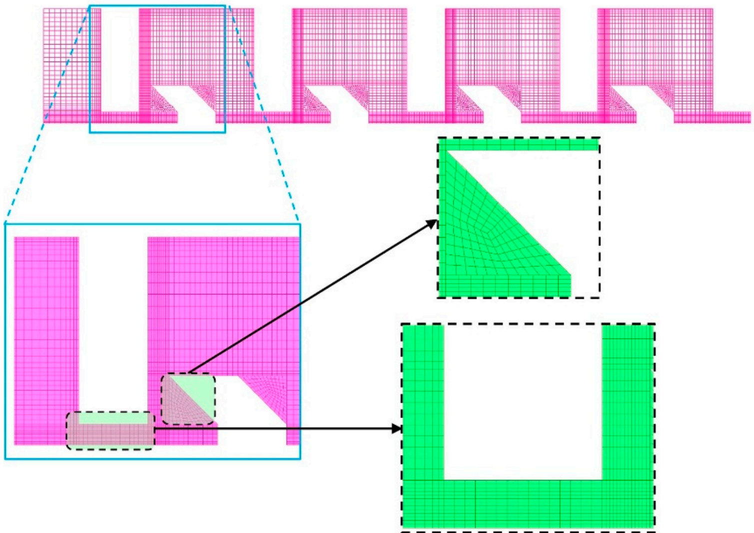

Figure 5. Mesh structure of SYLS.

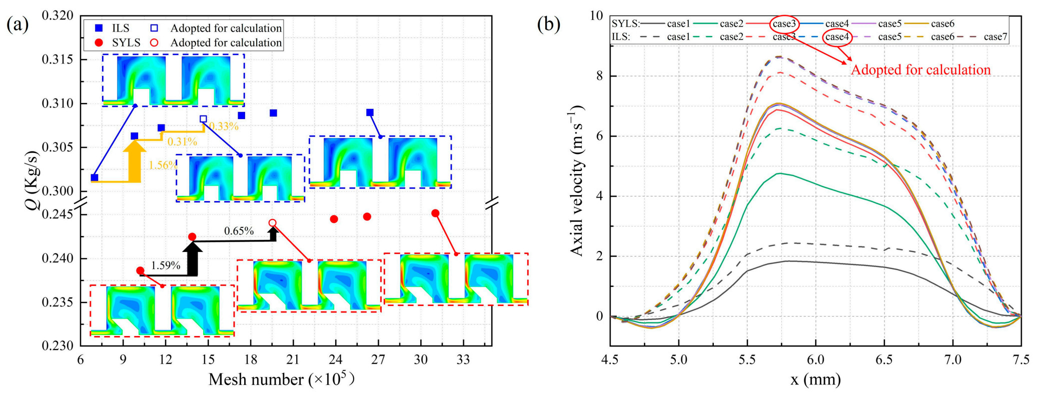

Figure 6. The mesh independence verification: (**a**) the effect of the number of meshes on leakage, (**b**) the effect of the number of meshes on axial velocity near rotor surface between rotor teeth.

4. Result and Discussion

For investigating the static characteristics of the SYLS structure, the effects of pressure drop, tilt angle, seal clearance, and the height of rotor teeth on leakage are calculated. Furthermore, the impacts of tilt angle and clearance on rotordynamic characteristics in different pressure drops and rotation speeds are also studied. Moreover, the whirl frequency ratio also is investigated to judge the stability of the SYLS structure.

4.1. Static Characteristics

4.1.1. Effects of Pressure Drop and Tilt Angle on Leakage

Figure 7 presents the effects of pressure drop and tilt angle on leakage of SYLS structure. The pressure drop is set from 0.1 MPa to 0.7 MPa, and the tilt angle is set from 45° to 135°. It can be seen from Figure 7a that the leakage increases with the increase in pressure drop at the same tilt angle. There is the same trend of variation of leakage in different tilt angles when the pressure drop increases from 0.1 MPa to 0.7 MPa. What can be clearly seen in Figure 7b is that the leakage presents a fluctuation phenomenon; it reaches the peak value at $\theta = 70°$. In other words, the static characteristics for SYLS structure at $\theta = 70°$ are the worst. When the tilt angle is larger than 90°, the leakage is lower than the angle of tilt less than 90°. In addition, it gets the trough value at $\theta = 135°$, which is about 30% lower than ILS.

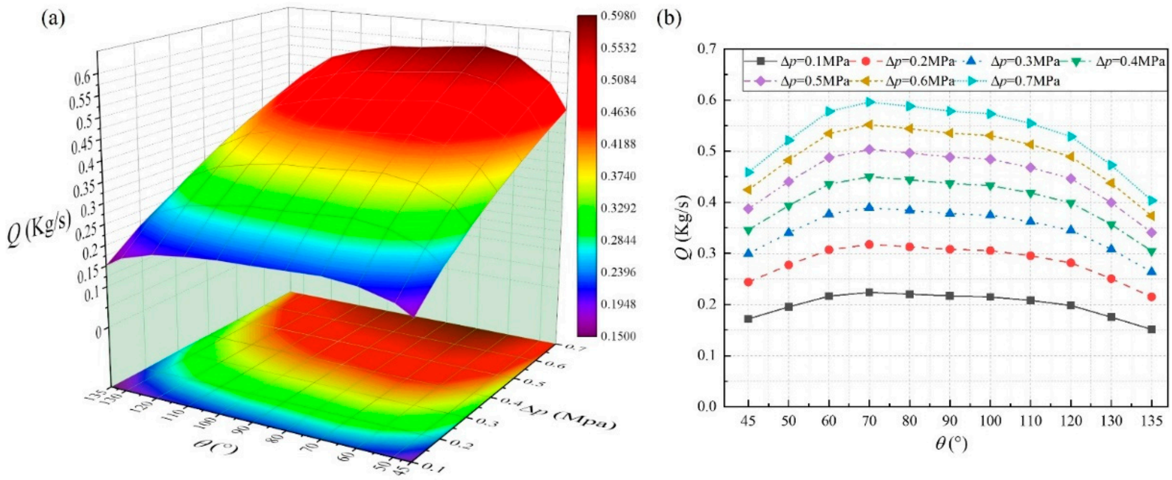

Figure 7. Effect of pressure drop and tilt angle on leakage: (**a**) 3D contour, (**b**) curve.

In order to investigate the difference in leakage caused by the tilt angles, the inner flow of the SYLS structure for different tilt angles at $\Delta p = 0.5$ MPa is calculated and analyzed. Figure 8 shows the static pressure distribution of four tilt angles (45°, 70°, 90°, and 135°). It indicates that the throttle function of narrow clearance causes the primary pressure drop. Accordingly, the static pressure of the cavity gradually decreases as the number of flows through the clearance increases. When the tilt angle deviates too much from 90°, the distance between the tip of rotor teeth and stator teeth may be as small as the clearance. Therefore, there is a second pressure drop at rotor teeth tips for SYLS structure at $\theta = 45°$ or $\theta = 135°$. As shown in Figure 9a,c, there are two main vortices in the cavity. When the rotor teeth tilt towards the stator teeth, the decrease in spacing between the rotor teeth and stator teeth generates a jet flow. It will cause larger right vortices in the cavity at $\theta = 45°$. Although the left vortices at $\theta = 90°$ are stronger than those at $\theta = 45°$, both vortices are limited by the size of the cavity. Therefore, the kinetic energy of the SYLS structure at $\theta = 45°$ is dissipated more completely, and the leakage is less. In contrast, the intensity of the right vortices is reduced with the increase in spacing between the rotor teeth and stator teeth, which results in the rise of leakage at $\theta = 70°$. From Figure 9, it is apparent that the SYLS structure at $\theta = 135°$ has the biggest vortices. A possible explanation for this phenomenon might be that the flow path is changed for the tilt angle, which is propitious for turbulent kinetic energy dissipation and vortices.

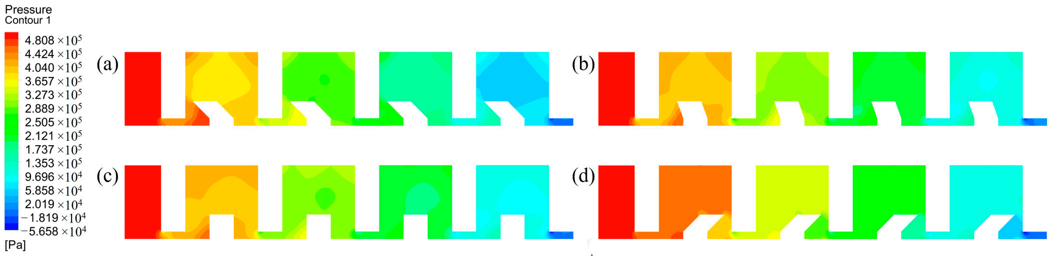

Figure 8. Static pressure contours at Δp = 0.5 MPa for different tilt angle (**a**) 45° (**b**) 70° (**c**) 90° and (**d**) 135°.

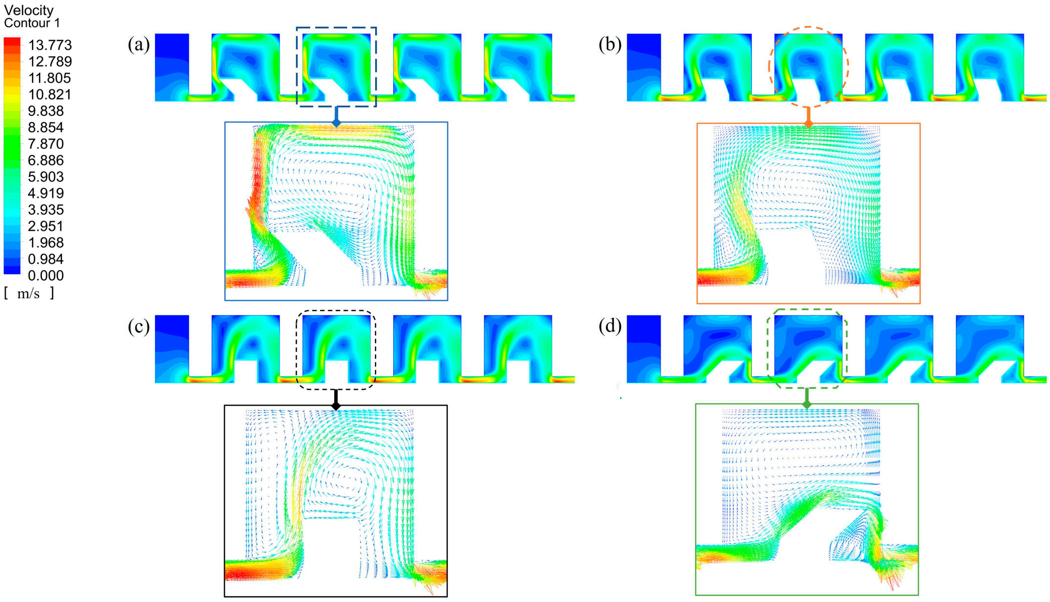

Figure 9. The velocity contours and corresponding vectors at Δp = 0.5 MPa for different tilt angles (**a**) 45° (**b**) 70° (**c**) 90° and (**d**) 135°.

4.1.2. Effects of Clearance on Leakage

Seal clearance is another key factor for leakage. In this paper, three different clearances (0.1 mm, 0.3 mm, and 0.5 mm) are selected to study the leakage performance of the SYLS structure with different tilt angles.

As Figure 10 shows, the leakage for different clearances increases with the increase in seal clearance. It can be seen from Figure 10a that when the seal clearance is 0.1 mm, the leakage is only a little different among different tilt angles for a given pressure drop. Furthermore, comparing the leakage at C_r = 0.1 mm and C_r = 0.5 mm, there is a dramatic phenomenon that the leakage of labyrinth seal extremely depends on clearance, especially the leakage rises by almost 80% when θ is 70°. Moreover, it also needs to be paid attention that the difference ratio of leakage is the least at θ = 135°. In other words, the static characteristics of SYLS at θ = 135° are the best on different tilt angles with the increase in clearance.

Figures 11 and 12 present the inner flow characteristics at Δp = 0.5 MPa for two clearances, 0.1 mm and 0.5 mm. As a small clearance case, a large pressure loss occurs after fluid flows through the clearance of stator teeth. A similar result also occurs for different tilt angles. As shown in Figure 12, the velocity in clearance rises when the clearance is small. Consequently, the turbulent kinetic energy dissipation is more effective in the cavity. However, in a larger clearance case, the high-velocity flow occupies the most domain of the cavity, resulting in smaller vortices. Therefore, as the clearance becomes larger, the leakage becomes greater. Moreover, Figure 12f reveals that the tips of rotor teeth appear to have pressure loss. When the distance between the rotor teeth tips and stator teeth is small, it works the same as the clearance of the stator teeth. For this reason, the static characteristics at θ = 135° are better than those of other structures.

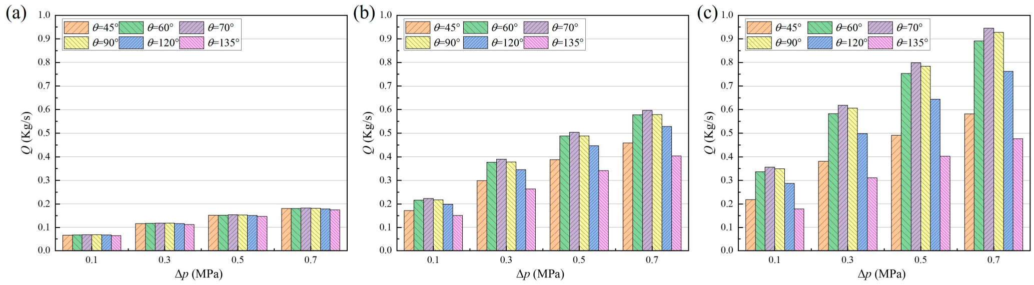

Figure 10. Effect of seal clearance on leakage: (**a**) C_r = 0.1 mm (**b**) C_r = 0.3 mm (**c**) C_r = 0.5 mm.

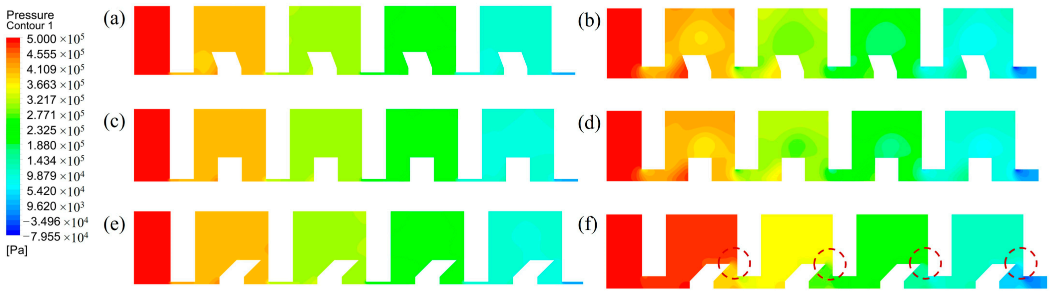

Figure 11. Static pressure contours at Δp = 0.5 MPa for two clearance: C_r = 0.1 mm (**a**) θ = 70° (**c**) θ = 90° (**e**) θ = 135°; C_r = 0.5 mm (**b**) θ = 70° (**d**) θ = 90° (**f**) θ = 135°.

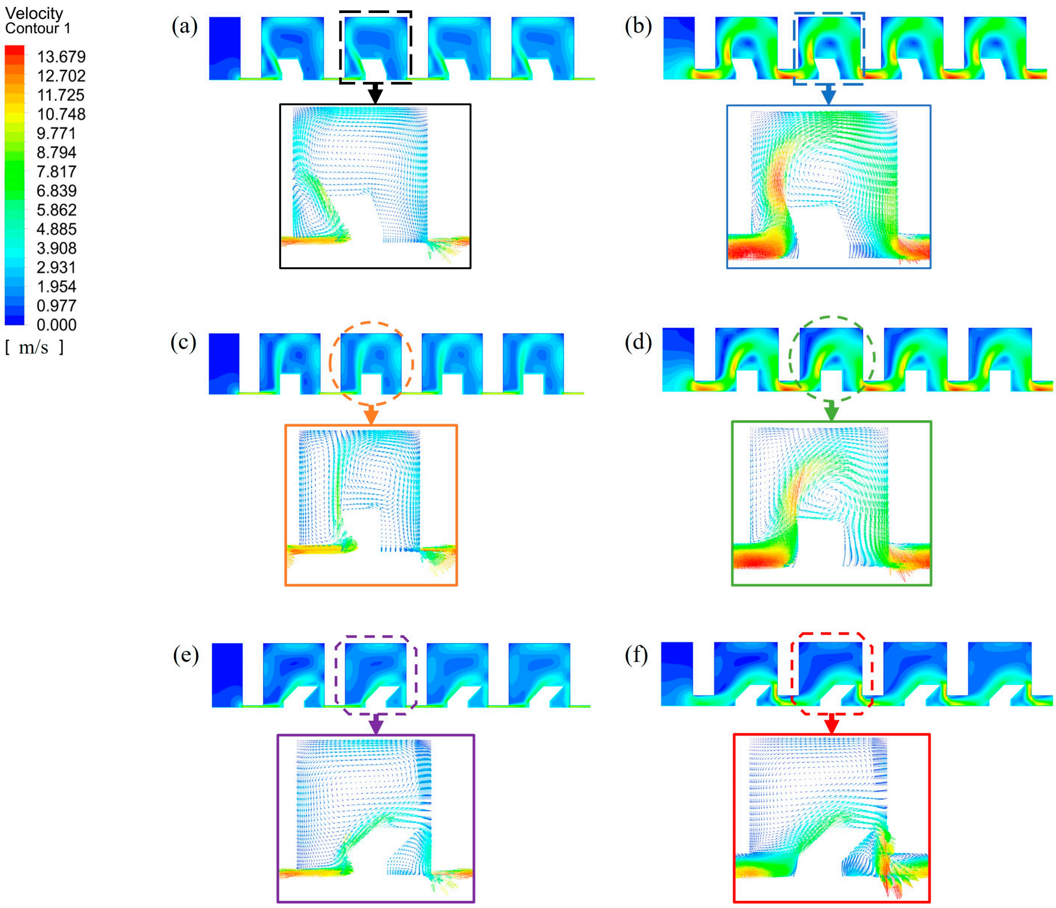

Figure 12. Velocity contours and corresponding vector plots at Δp = 0.5 MPa for different clearance: C_r = 0.1 mm (**a**) θ = 70° (**c**) θ = 90° (**e**) θ = 135°; C_r = 0.5 mm (**b**) θ = 70° (**d**) θ = 90° (**f**) θ = 135°.

4.1.3. Effects of the Height of Rotor Teeth on Leakage

Finally, the height of rotor teeth is selected as an independent variable to research the leakage performance, which transforms the clearance between the rotor teeth and the stator teeth when the rotor teeth are inclined. The effects of the height of rotor teeth on the leakage are separately plotted in Figure 13, which includes results for H_r = 0.8 mm, 1.0 mm, and 1.2 mm under conditions of different tilt angles and pressure drops. As the height of rotor teeth increases, there is a steep decrease at θ = 45° and θ = 135°, whereas it only has a slight decrease at the rest of the tilt angles.

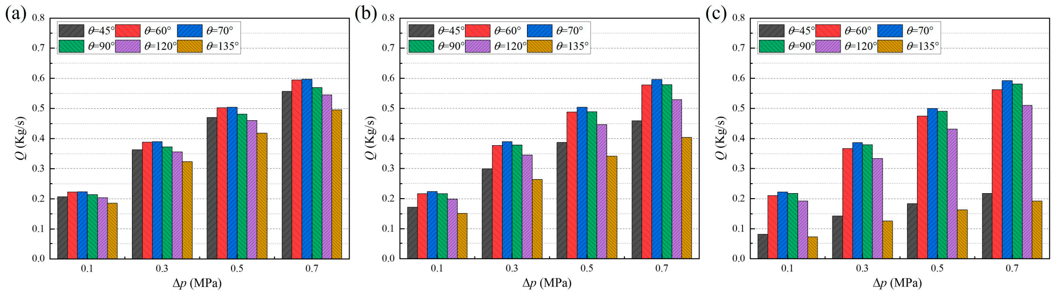

Figure 13. Effect of height of rotor teeth on leakage: (**a**) H_r = 0.8 mm (**b**) H_r = 1.0 mm and (**c**) H_r = 1.2 mm.

Figure 14 shows the static pressure contours at Δp = 0.5 MPa for different heights of rotor teeth. The distribution of static pressure is similar for three different heights at θ = 70°; therefore, the leakage is also similar. The height of rotor teeth determines the size of rotor tip clearance. The rotor tip clearance reduces with the increase in the height of the rotor tooth, which forms more pressure loss in the field. The velocity contours and vectors at Δp = 0.5 MPa for different heights of rotor teeth are shown in Figure 15. It can be seen that the small rotor tip clearance is good for turbulent kinetic energy dissipation and vortices. Accordingly, the leakage becomes less with the increase in the height of the rotor tooth at θ = 135°.

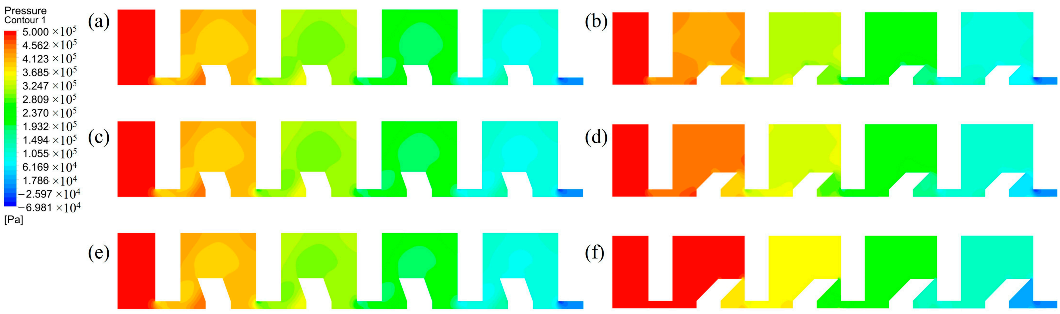

Figure 14. Static pressure contours at Δp = 0.5 MPa for different height of rotor teeth, θ = 70°: (**a**) H_r = 0.8 mm (**c**) H_r = 1.0 mm (**e**) H_r = 1.2 mm; θ = 135°: (**b**) H_r = 0.8 mm (**d**) H_r = 1.0 mm (**f**) H_r = 1.2 mm.

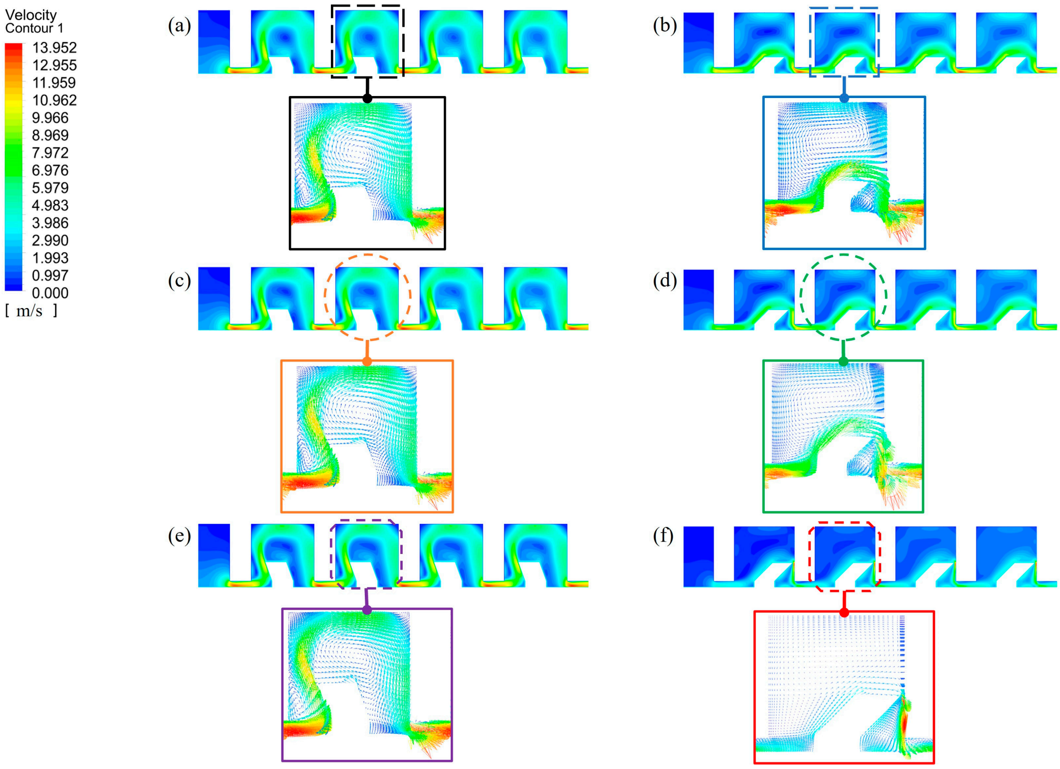

Figure 15. Velocity contours and corresponding vectors at Δp = 0.5 MPa for different height of rotor teeth, θ = 70°: (**a**) H_r = 0.8 mm (**c**) H_r = 1.0 mm (**e**) H_r = 1.2 mm; θ = 135°: (**b**) H_r = 0.8 mm (**d**) H_r = 1.0 mm (**f**) H_r = 1.2 mm.

4.2. Dynamic Characteristics

The rotordynamic model of the labyrinth seal is shown in Figure 16 at an eccentric state. r and t indicate the tangential and radial direction, respectively. The rotation and whirling speed are ω and Ω, respectively. The fluid-induced forces are modeled by:

$$-\begin{Bmatrix} F_x \\ F_y \end{Bmatrix} = \begin{bmatrix} K_{xx} & K_{xy} \\ K_{yx} & K_{yy} \end{bmatrix} \begin{Bmatrix} X \\ Y \end{Bmatrix} + \begin{bmatrix} C_{xx} & C_{xy} \\ C_{yx} & C_{yy} \end{bmatrix} \begin{Bmatrix} \dot{X} \\ \dot{Y} \end{Bmatrix} + \begin{bmatrix} M_{xx} & M_{xy} \\ M_{yx} & M_{yy} \end{bmatrix} \begin{Bmatrix} \ddot{X} \\ \ddot{Y} \end{Bmatrix} \quad (1)$$

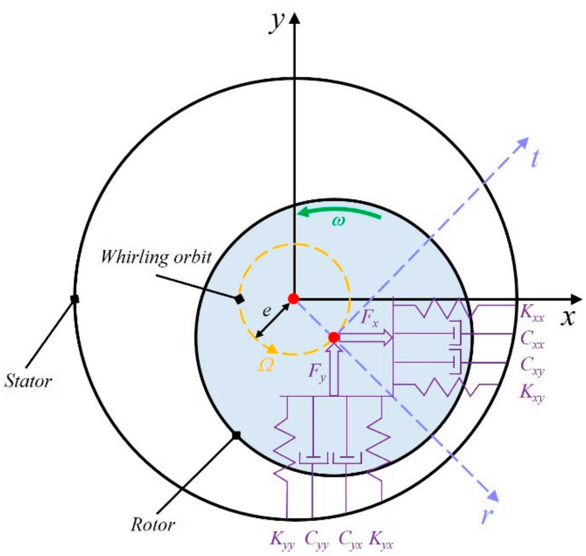

Figure 16. Rotordynamic model of labyrinth seal.

To simplify the computation, we assume that $K_{xx} = K_{yy} = K$, $K_{xy} = -K_{xy} = k$, $C_{xx} = C_{yy} = C$, $C_{xy} = -C_{yx} = c$, $M_{xx} = M_{yy} = M$, $M_{xy} = -M_{yx} = m$. Equation (1) is simplified Equation (2):

$$-\begin{Bmatrix} F_x \\ F_y \end{Bmatrix} = \begin{bmatrix} K & k \\ -k & K \end{bmatrix}\begin{Bmatrix} X \\ Y \end{Bmatrix} + \begin{bmatrix} C & c \\ -c & C \end{bmatrix}\begin{Bmatrix} \dot{X} \\ \dot{Y} \end{Bmatrix} + \begin{bmatrix} M & m \\ -m & M \end{bmatrix}\begin{Bmatrix} \ddot{X} \\ \ddot{Y} \end{Bmatrix} \tag{2}$$

Generally, there are three methods to calculate rotordynamic coefficients, which are the finite perturbation method [32], the whirling rotor method [24,33], and the transient simulation method [23]. When considering the complexity of transient analysis and moving mesh, the whirling rotor method is adopted in this paper. The whirling rotor method applies the moving reference frame (MRF) to determine the dynamic characteristics of the labyrinth seal. As shown in Figure 17, the rotor center is attached to the rotation frame; therefore, the transient analysis transforms the steady analysis. In the rotation coordinate system, the tangential component force F_t and radial component force F_r of the labyrinth seal are expressed in Equation (3) [27]:

$$\begin{cases} \frac{F_r}{e} = -K - c\Omega + M\Omega^2 \\ \frac{F_t}{e} = k - C\Omega \end{cases} \tag{3}$$

where the eccentric distance e is 5% of the clearance C_r in this paper, and the rotordynamic coefficients are determined by fitting multiple whirling frequencies. In the following calculation, the basic values are set as θ = 45°, C_r = 0.3 mm, Δp = 0.5 Mpa and ω = 3000 rpm. when two of the above parameters change, the other two parameters are kept the same.

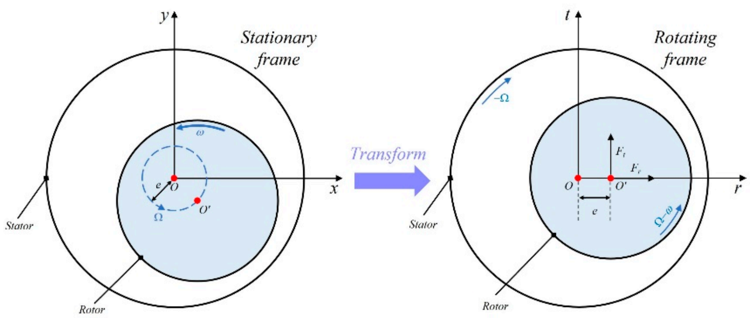

Figure 17. Frame transform from stationary to rotating.

4.2.1. Influence of Tilt Angle on Dynamic Coefficients for Different Pressure Drops and Rotation Speeds

Figure 18 presents the effect of tilt angle on the dynamic coefficients for different pressure drops and tilt angles. The direct stiffness K decreases with the increase in pressure drop. It is apparent that the direct stiffness of the SYLS structure at θ = 45° shows a sharp decline with the increase in pressure drop. However, the direct stiffness of the SYLS structure at θ = 135° reveals a slight sensitivity for pressure drop. As shown in Figure 8a,c, there is a great pressure drop between the upper side and lower side of the rotor teeth because of the throttling function generated by the tip of the rotor teeth. For the SYLS structure at θ = 45°, the pressure drop will generate a force in the same direction as the radial force, which may result in increasing direct stiffness related to the radial force.

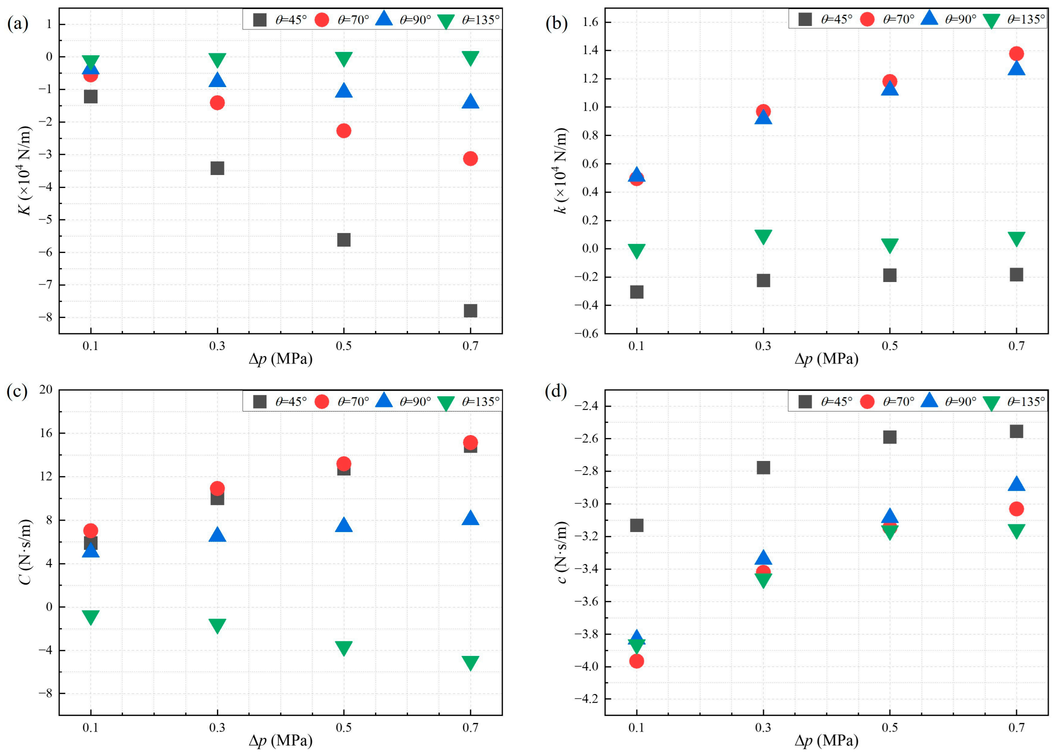

Figure 18. Dynamic coefficients for different pressure drops and tilt angles: (**a**) direct stiffness K, (**b**) cross-coupled stiffness k, (**c**) direct damping C and (**d**) cross-coupled damping c.

As the pressure drop increases, the cross-coupled stiffness k increases, which is the main factor for the nonsynchronous whirl. A large positive magnitude for k at $\theta = 90°$ and $\theta = 70°$ can aggravate the system instabilities for the SYLS structure, while the k changes little at $\theta = 135°$. Moreover, the negative k, which results in a positive effect on the stability of the sealing system [23], is indicated at $\theta = 45°$. One reason may be that the semi-Y rotor teeth structure causes the reverse tangential force component. Therefore, the cross-coupled stiffness, which is related to the tangential force component, becomes negative. The direct damping C, which displays the facility to restrain the unstable whirling motion, shows a similar tendency as the k except for the tilt angle $\theta = 135°$. The direct damping C at $\theta = 135°$ has an opposite tendency compared with other tilt angles, and it is even negative. It causes a stronger whirling motion and harms stability. In addition, the cross-coupled damping c increases as the pressure drop increases.

A detailed comparison of rotordynamic coefficients for different tilt angles and rotation speeds is furnished in Table 3. The rotation speed has negligible influence on the K for a certain tilt angle. It is interesting to note that there is a sharp decrease in the k at $\theta = 45°$ and $\theta = 135°$ compared with those at $\theta = 70°$ and $\theta = 90°$. A possible explanation for this might be that the SYLS structure at $\theta = 45°$ or $\theta = 135°$ strengthens high-speed flow near the rotor wall, which results in lower circumferential shear. The increasing rotation speed increases the k at $\theta = 70°$ and $\theta = 90°$, while it reduces the k at $\theta = 45°$ and $\theta = 135°$. For damping coefficients, the C slightly increases with the increase in rotation speed while the c presents an opposite tendency.

Table 3. The rotordynamic coefficients for different tilt angles and rotation speeds.

Tilt Angle θ (°)	Rotation Speed ω (rpm)	K (N/mm)	k (N/mm)	C (N·s/m)	c (N·s/m)
45	1000	−55.03	−0.17	12.08	−0.74
	2000	−55.45	−0.92	12.47	−1.66
	3000	−56.15	−1.86	12.72	−2.59
70	1000	−21.82	4.23	11.72	−0.94
	2000	−22.06	7.77	12.42	−2.01
	3000	−22.69	11.81	13.19	−3.15
90	1000	−10.23	3.83	9.28	−0.95
	2000	−10.40	7.12	10.06	−2.12
	3000	−10.88	11.20	11.14	−3.09
135	1000	0.72	0.63	−5.79	−1.19
	2000	0.62	0.62	−4.84	−2.19
	3000	−0.14	0.35	−3.63	−3.16

4.2.2. Influence of Clearance on Dynamic Coefficients for Different Pressure Drops or Rotation Speeds

The effect of clearance on dynamic coefficients for different pressure drops and rotation speeds is presented in Figure 19 and Table 4, respectively. It can be seen that all of the dynamic coefficients for different clearances increase with the increase in pressure drop except the K. When the clearance increases, the K fluctuates. As shown in Figure 19b, the pressure drop plays little effect on the k when the C_r increases from 0.3 mm to 0.5 mm. The same tendency is also presented in Ref. [22]. Moreover, the k and the C are the largest at C_r = 0.1 mm. The SYLS structure provides higher C with smaller clearance and higher rotation speed, and the lower k occurs in bigger clearance under the operational condition of 2000 rpm.

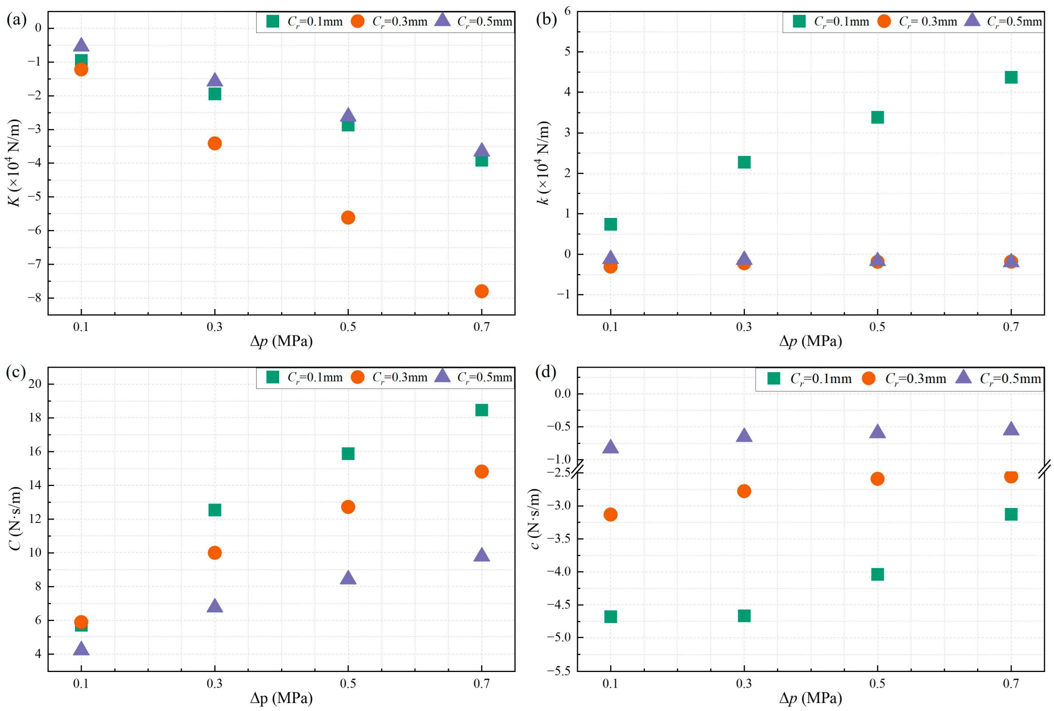

Figure 19. Dynamic coefficients for different pressure drops and clearances: (**a**) direct stiffness K, (**b**) cross-coupled stiffness k, (**c**) direct damping C and (**d**) cross-coupled damping c.

Table 4. The rotordynamic coefficients for various clearances and rotation speeds.

Clearance C_r (mm)	Rotation Speed ω (rpm)	K (N/mm)	k (N/mm)	C (N·s/m)	c (N·s/m)
0.1	1000	−23.99	22.93	14.07	−1.08
	2000	−25.88	28.36	15.40	−2.56
	3000	−28.71	33.83	15.89	−4.04
0.3	1000	−55.03	−0.17	12.08	−0.74
	2000	−55.45	−0.92	12.47	−1.66
	3000	−56.15	−1.86	12.72	−2.59
0.5	1000	−26.07	−1.50	8.18	−0.51
	2000	−26.64	−2.71	8.28	−1.15
	3000	−26.16	−1.68	8.43	−0.60

4.2.3. Whirl Frequency Ratio

The cross-coupled stiffness k and the direct damping C are crucial factors for stability among rotordynamic coefficients. In Refs. [34,35], the whirl frequency ratio, including the two parameters, is defined to compare the stability of different structures and operational conditions. The expression and corresponding criterion can be expressed as follows:

$$f = \frac{k}{C\omega} \tag{4}$$

$$\begin{cases} \forall(f > 1) \to \text{unstable} \\ \forall(0 < f \leq 1) \to \text{stable} \\ (f < 0) \to \text{stable, if } f(C > 0, k < 0) \end{cases} \tag{5}$$

Figure 20 shows the influence of four tilt angles on the whirl frequency ratio for different operational conditions. With the increase in the pressure drop, the whirl frequency ratio presents slight increases. However, the whirl frequency ratio shows fluctuation at θ = 135° and becomes negative at θ = 45°, which is useful for stabilizing the rotor seal system according to the stability criterion. Although the whirl frequency ratio also is negative at θ = 135°, it aggravates unstable, because the negative C and positive k can cause strong whirl. There is a small drop in the whirl frequency ratio with the increased rotation speed except for θ = 135°. In addition, an increasing trend with rotation speed implies a possible cross-frequency for SYLS structure at θ = 135°, which makes the whirl frequency ratio positive. It can be seen that the SYLS structure at θ = 70° is more stable than that at θ = 90°, which is irrespective of pressure drop and rotation speed. Moreover, the SYLS structure at θ = 45° presents the best stabilization among the four tilt angles.

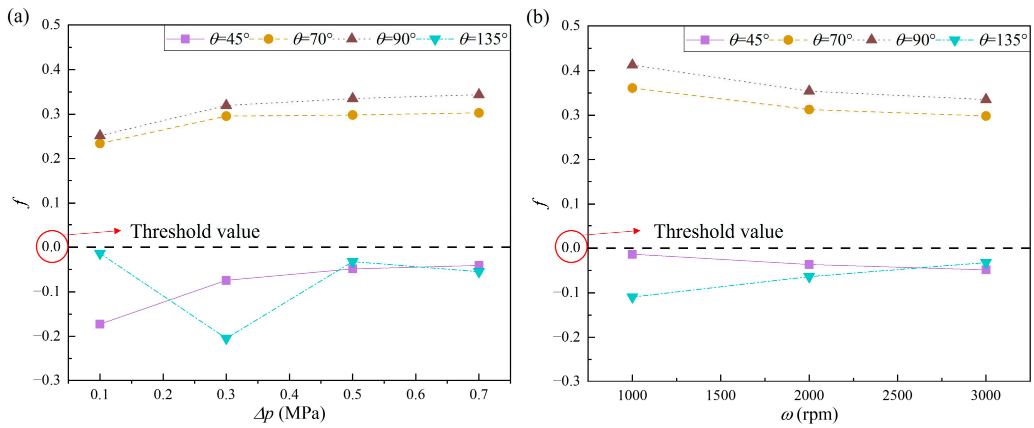

Figure 20. Influence of tilt angle on whirl frequency ratio for different operational conditions: (**a**) pressure drop and (**b**) rotation speed.

The effect of three clearances on the whirl frequency ratio for different operational conditions is depicted in Figure 21. It can be seen that the whirl frequency ratio is sensitive to pressure drop and rotation speed at C_r = 0.1 mm. As pressure drop increases, the whirl frequency ratio rises; therefore, the stability of the SYLS structure becomes poor. The whirl frequency ratio is larger than one at ω = 1000 rpm, which means that the system is unstable. Moreover, the whirl frequency ratio remains negative and steady, whatever the pressure drop and rotation speed change at C_r = 0.3 mm and C_r = 0.5 mm.

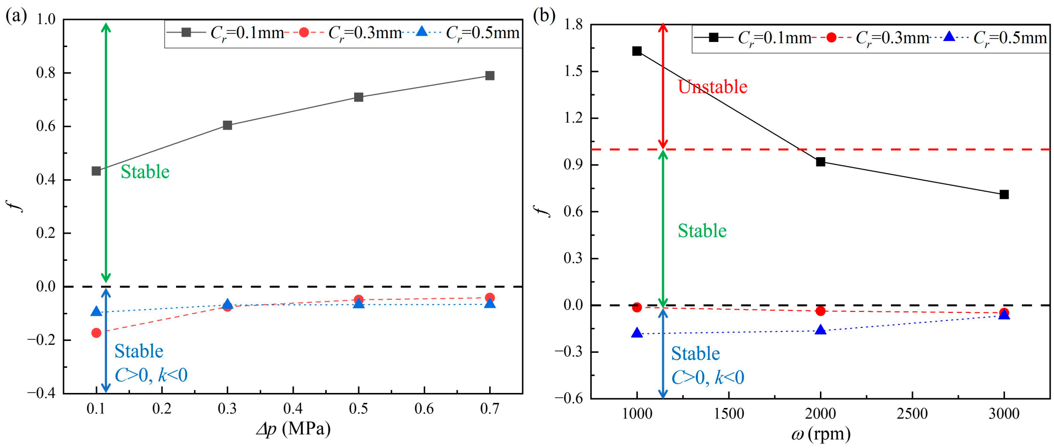

Figure 21. Effect of clearance on whirl frequency ratio at different operational conditions: (**a**) pressure drop and (**b**) rotation speed.

5. Conclusions

In this paper, a novel SYLS structure is proposed to minimize leakage based on the ILS. The influences of pressure drop, tilt angle, clearance, and height of rotor teeth on the static and dynamic characteristics are studied for SYLS structure. In addition, the whirl frequency ratio is also studied to present the stability performance of different SYLS structures. The main conclusions are as follows:

(1) The numerical results calculated by the standard k-ε turbulent model present a good agreement with the experimental results. The maximum error and minimum errors are 2.81% and 1.87%, respectively.

(2) The leakage increases with the increase in pressure drop and clearance. However, the leakage presents the trend of secondary curves, and it reaches the peak value at θ = 70°; in other words, the leakage performance is the worst for the SYLS structure at θ = 70°. In addition, the leakage gets the trough value at θ = 135°, which is about 30% lower than ILS.

(3) The direct stiffness K of the SYLS structure at θ = 45° shows a sharp decline with the increase in pressure drop, while it reveals a slight sensitivity at θ = 135°. The reason is that the throttling function generated by the tip of rotor teeth causes a great pressure drop between the upper side and lower side of the rotor teeth, which changes the radial force. The dynamic coefficients for different clearances increase with the increase in pressure drop except for the direct stiffness K. Moreover, the cross-coupled stiffness k and the direct damping C are the largest at C_r = 0.1 mm.

(4) The low-pressure drop and high rotation speed can induce a small whirl frequency ratio, which is helpful for the stability of the SYLS structure. The SYLS structure presents the best stability performance at θ = 45°. In addition, the whirl frequency ratio is sensitive to pressure drop and exceeds one under the conditions of C_r = 0.1 mm and ω = 1000 rpm.

Author Contributions: Conceptualization, H.S., W.Z. and J.S.; methodology, H.S. and W.Z.; software, H.S.; validation, H.S. and W.Z.; formal analysis, H.S. and W.Z.; investigation, H.S.; resources, W.Z. and J.S.; data curation, H.S.; writing—original draft preparation, H.S. and W.Z.; writing—review and editing, W.Z. and J.S.; visualization, H.S.; supervision, W.Z.; project administration, W.Z. and J.S.; funding acquisition, W.Z. and J.S. All authors have read and agreed to the published version of the manuscript.

Funding: The research was funded by the Project funded by China Postdoctoral Science Foundation (Grant No. 2018M642177), the Sichuan Provincial Key Lab of Process Equipment and Control (Grant No. GK201902) and the Zhejiang Postdoctoral Preferential Foundation (Grant No. zj2018009).

Data Availability Statement: Not applicable.

Conflicts of Interest: The authors declare no conflict of interest.

Nomenclature

H_s	Stator tooth height (mm)
H_r	Rotor tooth height (mm)
H_v	Vertical height of rotor tooth (mm)
C_r	Tip clearance (mm)
D	Rotor diameter (mm)
L	Seal length (mm)
L_p	Pitch between rotor teeth and static teeth (mm)
B_s	Stator tooth width (mm)
B_r	Rotor tooth width (mm)
B_c	Cavity width (mm)
θ	Tilt angle (°)
Z	Tooth number
Q	Leakage (kg/s)
Δp	Pressure drop (MPa)
Ω	Whirling speed (rpm)
ω	Rotating speed (rpm)
F_x, F_y	Seal reaction force in x and y axis (N)
F_r, F_t	Seal reaction force in radial and tangential direction (N)
K_{xx}, K_{yy}	Direct stiffness coefficient in x and y direction (N/m)
K_{xy}, K_{yx}	Cross-coupled stiffness coefficient in x and direction (N/m)
C_{xx}, C_{yy}	Direct damping coefficient in x and y direction (N·s/m)
C_{xy}, C_{yx}	Cross-coupled damping coefficient in x and y direction (N·s/m)
M_{xx}, M_{yy}	Direct added mass in x and y direction (kg)
M_{xy}, M_{yx}	Cross-coupled added mass in x and y direction (kg)
K	Direct stiffness coefficient (N/m)
k	Cross-coupled stiffness coefficient (N/m)
C	Direct damping coefficient (N·s/m)
c	Cross-coupled damping coefficient (N·s/m)
M	Direct added mass (kg)
m	Cross-coupled added mass (kg)
f	Whirl frequency ratio

References

1. Lei, C.; Yiyang, Z.; Zhengwei, W.; Yexiang, X.; Ruixiang, L. Effect of Axial Clearance on the Efficiency of a Shrouded Centrifugal Pump. *J. Fluids Eng.* **2015**, *137*, 071101. [CrossRef]
2. Zhou, W.; Qiu, N.; Wang, L.; Gao, B.; Liu, D. Dynamic Analysis of a Planar Multi-Stage Centrifugal Pump Rotor System Based on a Novel Coupled Model. *J. Sound Vib.* **2018**, *434*, 237–260. [CrossRef]
3. Zhou, W.; Yu, D.; Wang, Y.; Shi, J.; Gan, B. Research on the Fluid-induced Excitation Characteristics of the Centrifugal Pump Considering the Compound Whirl Effect. *Facta Univ. Ser. Mech. Eng.* **2021**. [CrossRef]
4. Li, Y.; Wang, Y.; Dai, X.; Wang, Z. Sensitivity of different sealing structures to axial movement of centrifugal pump impeller. *J. Drain Irrig Mach Eng.* **2021**, *39*, 122–127. [CrossRef]
5. Feng, J.; Wang, L.; Yang, H.; Peng, X. Numerical Investigation on the Effects of Structural Parameters of Labyrinth Cavity on Sealing Performance. *Math. Probl. Eng.* **2018**, *2018*, 5273582. [CrossRef]
6. Cao, H.; Zhang, W.; Yin, L.; Yang, L. Numerical Study of Leakage and Rotordynamic Performance of Staggered Labyrinth Seals Working with Supercritical Carbon Dioxide. *Shock Vib.* **2022**, *2022*, 3896212. [CrossRef]

7. Lee, S.I.; Kang, Y.J.; Kim, W.J.; Kwak, J.S.; Kim, T.S.; Kim, D.H.; Jung, I.Y. Effects of Tip Clearance, Number of Teeth, and Tooth Front Angle on the Sealing Performance of Straight and Stepped Labyrinth Seals. *J. Mech. Sci. Technol.* **2021**, *35*, 1539–1547. [CrossRef]
8. Hur, M.S.; Lee, S.I.; Moon, S.W.; Kim, T.S.; Kwak, J.S.; Kim, D.H.; Jung, I.Y. Effect of Clearance and Cavity Geometries on Leakage Performance of a Stepped Labyrinth Seal. *Processes* **2020**, *8*, 1496. [CrossRef]
9. Andrés, L.S.; Wu, T.; Barajas-Rivera, J.; Zhang, J.; Kawashita, R. Leakage and Cavity Pressures in an Interlocking Labyrinth Gas Seal: Measurements Versus Predictions. *J. Eng. Gas Turbines Power* **2019**, *141*, 101007. [CrossRef]
10. Zhang, M.; Yang, J.; Xu, W.; Xia, Y. Leakage and Rotordynamic Performance of a Mixed Labyrinth Seal Compared with That of a Staggered Labyrinth Seal. *J. Mech. Sci. Technol.* **2017**, *31*, 2261–2277. [CrossRef]
11. Woo, S.; Jang, H.; Kwak, H.; Moon, Y.; Kim, C. Leakage Analysis of Helical Grooved Pump Seal Using CFD. *J. Mech. Sci. Technol.* **2020**, *34*, 4183–4191. [CrossRef]
12. Wróblewski, W.; Fraczek, D.; Marugi, K. Leakage Reduction by Optimisation of the Straight–through Labyrinth Seal with a Honeycomb and Alternative Land Configurations. *Int. J. Heat Mass Transf.* **2018**, *126*, 725–739. [CrossRef]
13. Szymański, A.; Wróblewski, W.; Bochon, K.; Majkut, M.; Strozik, M.; Marugi, K. Experimental Validation of Optimised Straight-through Labyrinth Seals with Various Land Structures. *Int. J. Heat Mass Transf.* **2020**, *158*, 119930. [CrossRef]
14. Wu, T.; Andrés, L.S. Gas Labyrinth Seals: Improved Prediction of Leakage in Gas Labyrinth Seals Using an Updated Kinetic Energy Carry-Over Coefficient. *J. Eng. Gas Turbines Power* **2020**, *142*, 121012. [CrossRef]
15. Dogu, Y.; Sertçakan, M.C.; Bahar, A.S.; Pişkin, A.; Arıcan, E.; Kocagül, M. Computational Fluid Dynamics Investigation of Labyrinth Seal Leakage Performance Depending on Mushroom-Shaped Tooth Wear. *J. Eng. Gas Turbines Power* **2016**, *138*, 032503. [CrossRef]
16. Li, Z.; Li, J.; Yan, X.; Feng, Z. Effects of Pressure Ratio and Rotational Speed on Leakage Flow and Cavity Pressure in the Staggered Labyrinth Seal. *J. Eng. Gas Turbines Power* **2011**, *133*, 114503. [CrossRef]
17. Joachimiak, D.; Krzyślak, P. Analysis of the Gas Flow in a Labyrinth Seal of Variable Pitch. *J. Appl. Fluid Mech.* **2019**, *12*, 921–930. [CrossRef]
18. Nagai, K.; Koiso, K.; Kaneko, S.; Taura, H.; Watanabe, Y. Numerical and Experimental Analyses of Static and Dynamic Characteristics for Partially Helically Grooved Liquid Annular Seals. *J. Tribol.* **2019**, *141*, 022201. [CrossRef]
19. Li, Z.; Li, J.; Feng, Z. Numerical Comparisons of Rotordynamic Characteristics for Three Types of Labyrinth Gas Seals with Inlet Preswirl. *Proc. Inst. Mech. Eng. Part J. Power Energy* **2016**, *230*, 721–738. [CrossRef]
20. Zhang, W.; Gu, Q.; Wang, T. Study on the Rotordynamic Performance of a Novel Anti-Stagnation Labyrinth Seal. *J. Vib. Eng. Technol.* **2020**, *8*, 835–846. [CrossRef]
21. Alex Moreland, J.; Childs, D.W.; Bullock, J.T. Measured Static and Rotordynamic Characteristics of a Smooth-Stator/Grooved-Rotor Liquid Annular Seal. *J. Fluids Eng.* **2018**, *140*, 101109. [CrossRef]
22. Zhang, M.; Childs, D.W.; Tran, D.L.; Shresth, H. Effects of Clearance on the Performance of a Labyrinth Seal Under Wet-Gas Conditions. *J. Eng. Gas Turbines Power* **2020**, *142*, 111012. [CrossRef]
23. Li, Z.; Li, J.; Feng, Z. Numerical Comparison of Rotordynamic Characteristics for a Fully Partitioned Pocket Damper Seal and a Labyrinth Seal With High Positive and Negative Inlet Preswirl. *J. Eng. Gas Turbines Power* **2016**, *138*, 042505. [CrossRef]
24. Zhang, W.; Gu, Q.; Cao, H.; Wang, Y.; Yin, L. Improving the Rotordynamic Stability of Short Labyrinth Seals Using Positive Preswirl. *J. Vibroengineering* **2020**, *22*, 1295–1308. [CrossRef]
25. Untaroiu, A.; Jin, H.; Fu, G.; Hayrapetiau, V.; Elebiary, K. The Effects of Fluid Preswirl and Swirl Brakes Design on the Performance of Labyrinth Seals. *J. Eng. Gas Turbines Power* **2018**, *140*, 082503. [CrossRef]
26. Wu, T.; San Andrés, L. Pump Grooved Seals: A Computational Fluid Dynamics Approach to Improve Bulk-Flow Model Predictions. *J. Eng. Gas Turbines Power* **2019**, *141*, 101005. [CrossRef]
27. Zhai, L.; Wu, G.; Wei, X.; Qin, D.; Wang, L. Theoretical and Experimental Analysis for Leakage Rate and Dynamic Characteristics of Herringbone-Grooved Liquid Seals. *Proc. Inst. Mech. Eng. Part J J. Eng. Tribol.* **2015**, *229*, 849–860. [CrossRef]
28. Zhai, L.; Zhenjie, Z.; Zhonghuang, C.; Jia, G. Dynamic Analysis of Liquid Annular Seals with Herringbone Grooves on the Rotor Based on the Perturbation Method. *R. Soc. Open Sci.* **2018**, *5*, 180101. [CrossRef] [PubMed]
29. Zhai, L.; Chi, Z.; Guo, J.; Zhang, Z.; Zhu, Z. Theoretical Solutions for Dynamic Characteristics of Liquid Annular Seals with Herringbone Grooves on the Stator Based on Bulk-Flow Theory. *Sci. Technol. Nucl. Install.* **2018**, *2018*, 1–13. [CrossRef]
30. Jia, X.; Zheng, Q.; Jiang, Y.; Zhang, H. Leakage and Rotordynamic Performance of T Type Labyrinth Seal. *Aerosp. Sci. Technol.* **2019**, *88*, 22–31. [CrossRef]
31. Zhou, W.; Zhao, Z.; Wang, Y.; Shi, J.; Gan, B.; Li, B.; Qiu, N. Research on Leakage Performance and Dynamic Characteristics of a Novel Labyrinth Seal with Staggered Helical Teeth Structure. *Alex. Eng. J.* **2021**, *60*, 3177–3187. [CrossRef]
32. Zhang, E.; Jiao, Y.; Chen, Z. Dynamic Behavior Analysis of a Rotor System Based on a Nonlinear Labyrinth-Seal Forces Model. *J. Comput. Nonlinear Dyn.* **2018**, *13*, 101002. [CrossRef]
33. Tsukuda, T.; Hirano, T.; Watson, C.; Morgan, N.R.; Weaver, B.K.; Wood, H.G. A Numerical Investigation of the Effect of Inlet Preswirl Ratio on Rotordynamic Characteristics of Labyrinth Seal. *J. Eng. Gas Turbines Power* **2018**, *140*, 082506. [CrossRef]
34. Rotordynamic Characteristics of Rotating Labyrinth Gas Turbine Seal with Centrifugal Growth. *Tribol. Int.* **2016**, *97*, 349–359. [CrossRef]
35. Iwatsubo, T.; Ishimaru, H. Consideration of Whirl Frequency Ratio and Effective Damping Coefficient of Seal. *J. Syst. Des. Dyn.* **2010**, *4*, 177–188. [CrossRef]